Equilibrium segregation patterns and alloying in Cu/Ni nanoparticles: Experiments versus modeling

M. Hennes,[1,2,*] J. Buchwald,[1] U. Ross,[1] A. Lotnyk,[1] and S. G. Mayr[1,2,3,†]

[1]*Leibniz Institute of Surface Modification, Permoserstr. 15, 04318 Leipzig, Germany*

[2]*Translational Centre for Regenerative Medicine, University of Leipzig, Philipp-Rosenthal-Str. 55, 04103 Leipzig, Germany*

[3]*Faculty of Physics and Earth Sciences, University of Leipzig, Linnéstr. 5, 04103 Leipzig, Germany*

(Received 17 February 2015; revised manuscript received 9 April 2015; published 1 June 2015)

We analyze the segregation behavior of bimetallic nanoparticles (NPs) with moderate miscibility gap by applying a combined experimental/simulation approach to Cu/Ni as a model system. Using a hybrid molecular dynamics/Metropolis Monte Carlo algorithm (MD/MMC) based on the embedded atom method (EAM), we derive the equilibrium distribution of atomic species in the clusters for varying concentrations and particle structures. To cross-check the predictive power of our approach, we compare these results with modified EAM (MEAM) and density functional theory based *ab initio* calculations. This permits to identify possible shortcomings of the EAM when used to describe bimetallic NPs. Additionally, we isolate vibrational entropy contributions to the free energy of the NPs and special focus is put on the possibility of entropic stabilization of segregated versus solid solution NPs. Finally, we complement our simulations by experimental results, which are obtained by studying the behavior of plasma gas condensation synthesized Ni@Cu core-shell (CS) particles upon annealing.

DOI: 10.1103/PhysRevB.91.245401 PACS number(s): 61.46.Bc, 61.46.Hk, 63.22.Kn, 66.30.Pa

I. INTRODUCTION

Segregation phenomena and phase separation in weakly miscible multicomponent metallic nanoparticles (NPs) have been the focus of intensive research efforts in recent years. In contrast to their bulk counterparts, phase diagrams of bimetallic nanoparticles can exhibit a greater degree of complexity, owing to the variety of segregation patterns that can be obtained in these small systems. These include rotationally symmetric nanophases like core-shell (CS) or onionlike (ON) as well as structures lacking this symmetry, e.g., of Janus (JA) or dumbbell type (DB) [1].

Still, a thorough theoretical understanding of the underlying physical mechanisms yielding these patterns is far from being reached. Some key aspects—differences in surface free energy, for example—are established to play a crucial role in selected processes like surface segregation. Nevertheless, it remains a challenge to predict the occurrence of certain demixed states from knowledge of a given set of material parameters only. Theoretical modeling is further impeded by the variety of polyhedral structures that can be adopted in systems consisting only of several thousand atoms and the complexity of the resulting energy landscapes.

Despite these difficulties, recent computer simulations have permitted to identify general principles underlying segregation in weakly miscible bimetallic NPs. In particles with icosahedral structure, the atomic species with the smaller lattice constant has been predicted to be placed in the center of the NP. This was shown for Ag/Cu, Ag/Ni, Ag/Co, and Au/Co, with a morphological instability developing when crossing a critical concentration and resulting in asymmetric cores [2]. In fcc nanocrystals, on the other hand, a concentration dependent behavior was reported [3,4]. There, computer modeling yielded either preferential placement of "smaller" atoms in the subsurface layer (giving rise to ON equilibrium structures as seen for Cu/Co or Au/Pt), or asymmetric JA-like structures [2].

However, a discrepancy persists between the significant amount of modeling results on segregation and the limited number of experiments. With regard to temperature-induced segregation pattern transitions, few theoretical predictions on weakly miscible systems could be explicitly verified in the laboratory so far, with the most prominent example being Ag/Cu [5]. For many other systems, exhaustive experimental investigations are not available to date [6].

This is astonishing, as there is tremendous interest in design of multicomponent NPs in such different fields as catalysis, data storage, and especially medicine, where well tailored, biocompatible magnetic NPs can be employed for imaging, diagnostic or curative purposes [7]. Here, a thorough understanding of nanoalloy phase diagrams could not only pave the way for new synthesis strategies relying on self organization, but must also generally be considered as a prerequisite for any application with pronounced structure-functionality interdependence. This especially holds with regard to the variety of recently developed gas phase techniques, that allow for the production of bimetallic out-of-equilibrium structures [8,9]. Studying the thermal stability of these particles and unveiling their transformation paths to equilibrium is certainly one of the great challenges of ongoing nanoalloy research.

In the present work, we use Cu/Ni as a model system with a small miscibility gap. Although its bulk and thin film behavior have been extensively studied, less is known about structural properties of demixed Cu/Ni particles so far. Previous experimental studies have primarily focused on analysis of alloyed NPs [10–12]. Here, we put segregated structures under scrutiny, from a theoretical/simulation, as well as from an experimental perspective.

We therefore proceed as follows: in a first step, we employ a hybrid molecular dynamics/Metropolis Monte Carlo (MD/MMC) algorithm based on the well established embedded atom method (EAM) [13] to determine equilibrium

*marcel.hennes@iom-leipzig.de

†stefan.mayr@iom-leipzig.de

segregation patterns of Cu/Ni NPs. As our algorithm selectively excludes vibrational entropy contributions to the free energy, we explicitly demonstrate that vibrational entropy can be neglected, when studying equilibrium demixed particle configurations in this material system. In a third part of this work, we proceed to analyze in greater detail the significance of onion-like segregation patterns, which are predicted by our EAM based approach. This is achieved by cross-checking our EAM based findings with the modified EAM (MEAM) [14] and *ab initio* calculations. Finally, we compare our theoretical predictions with annealing results of plasma gas condensation synthesized Ni@Cu CS-NPs.

II. METHODS

A. Computer modeling

1. EAM based hybrid molecular dynamics/Metropolis Monte Carlo simulations

In the present work, we simulated Cu/Ni nanoparticle equilibrium configurations along the lines of a recent study, using a hybrid simulation approach [15]. Our modeling scheme is based on the alternate use of Monte Carlo atom type exchanges and short molecular dynamics (MD) simulations for structural relaxation, employing a self-developed code.

To describe interatomic interactions, we used the EAM formalism. As shown in previous studies, comparison of different potentials yielded comparable segregation patterns in equiatomic Cu/Ni fcc nanocrystals [15]. For calculation of NP equilibrium configurations, we chose the EAM potential developed by Johnson [16], primarily because its mixing enthalpy was found closer to experimental values. In every MD run, we solved the equations of motion with a fifth-order Gear predictor-corrector scheme, while thermalization was attained with the help of a Berendsen thermostat. The length of every MD run was fixed to $\Delta t_{\mathrm{MD}} = 2$ ps, yielding a good compromise between simulation speed and stress relaxation. For all MD runs, we placed the particle of interest in a cubic simulation box with fixed edge length $L = 20\,a$, $a = 3.52$ Å being the lattice constant of Ni at 0 K.

Following every MD run, the average internal energy of the particle in a new configuration (resulting from atom exchange prior to the MD run) was calculated and used as an input for the Metropolis algorithm. As known from the classical MMC scheme, any newly proposed configuration was accepted, if the energy in the new configuration was lowered. On the other hand, if the energy was raised, it was accepted with probability $e^{\frac{\Delta E}{kT}}$, ΔE being the energy difference between the old and the new configuration. For phase space sampling, we used between 50 000 and 150 000 hybrid steps (consisting of alternate atom exchanges and MD runs). Depending on NP size, we thus attained total MD simulation times of up to 300 ns.

Initial particle configurations required for our algorithm were obtained as follows: we cut all spherical fcc crystallites out of a larger block of Ni atoms at 0 K; decahedral and icosahedral particles were built using NPSTUDIO v.3 [17]. In addition to these structures, the impact of grain boundaries on phase separation was also studied. This was achieved by constructing particles with one twist boundary. The twist was created in a cell of 4000 Ni atoms at 0 K, by dividing the latter into two equal parts along the (001) plane, which were subsequently rotated against each other. After relaxation, we cut spherical particles out of the block and additionally relaxed them for another 200 ps. Finally, atom positions were assigned randomly to Ni or Cu until obtaining the desired concentration in the particles. For every concentration and structure, we performed multiple hybrid simulation runs in order to ensure that the initial placement of atoms on the lattice did not affect the resulting equilibrium configuration.

2. Vibrational entropy determination

All vibrational entropy calculations in our work rely on the harmonic approximation [18]:

$$S_{\mathrm{vib}} = 3k_{\mathrm{B}} \int_0^\infty \rho(\epsilon)[(n(\epsilon)+1)\ln(n(\epsilon)+1) - n(\epsilon)\ln(n(\epsilon))]d\epsilon \quad (1)$$

with the Planck distribution $n(\epsilon) = (e^{\epsilon/k_{\mathrm{B}}T} - 1)^{-1}$ and $\rho(\epsilon)$ being the phonon density of states (PDOS). To assess the PDOS, we performed MD runs of total length $t = 160$ ps at $T = 300$ K. While the first 80 ps were systematically discarded and only served to ensure full relaxation, the second half of every simulation run was used to calculate the velocity autocorrelation function $\langle \mathbf{v}(0)\mathbf{v}(t)\rangle$. From this quantity, we then obtained the PDOS after normalization using a fast Fourier transformation.

Along the same lines, we also calculated the excess heat capacity $\Delta c = c^{\mathrm{NP}} - c^{\mathrm{bulk}}$, primarily for comparison with literature results:

$$c = 3k_{\mathrm{B}} \int_0^\infty \rho(\epsilon)\left[\left(\frac{\epsilon n(\epsilon)}{k_{\mathrm{B}}T}\right)^2 e^{\epsilon/k_{\mathrm{B}}T}\right] d\epsilon. \quad (2)$$

To check the predictive power and reliability of our implementation, we simulated bulk PDOS, employing cubic cells of total size $N = 32\,000$ atoms for Cu and Ni. Additionally, spherical elemental Cu and Ni nanocrystals with $N = 532$ were studied. Finally, four bimetallic spherical nanocrystals, as depicted in Fig. 3(c) have been analyzed for three different concentrations, employing the aforementioned simulation protocol. In all cases, special care was taken to achieve a vanishing total angular momentum of the clusters.

Because the analytical Johnson potential used in this study for computation of particle equilibrium structures is known to possess some minor shortcomings with regard to the description of elastic properties, we cross checked the bulk and elemental particle vibrational behavior by using a second EAM parameterization [19].

3. MEAM and ab initio calculations

To complement our modeling based on the EAM, we performed additional simulations using the modified EAM (MEAM) as well as density functional calculations. These computations served the specific purpose of analyzing the significance of Ni subsurface placement in low temperature equilibrium Cu/Ni configurations. This is achieved by computation of the energetics and relaxation of slabs consisting of ten atomic layers with different Cu and Ni placement (subsurface versus bulk), as will be described in detail.

The modified EAM approach (MEAM) is employed [14,20] to put under scrutiny the impact of directional bonding in the presence of surfaces. As an enhancement of the EAM formalism, it introduces an angular dependency of the electron density function ρ yielding significant advantages over classical EAM treatments. In our computations, we used a MEAM potential recently developed for Cu/Ni [21]. All simulations related to MEAM were performed using LAMMPS [22], as our code, employed for hybrid MD/MMC computations, is only optimized for the EAM. For thermalization, we used a Nosé-Hoover thermostat at a temperature of 0.1 K; a typical runtime of 5 ps was chosen to achieve full relaxation.

We additionally conducted *ab initio* DFT calculations of Cu/Ni surfaces by employing the QUANTUM ESPRESSO [23] software package. For all computations, ultrasoft pseudopotentials [24] from QUANTUM ESPRESSO [25] were used, all of them based on the GGA-PBE exchange-correlation functional [26]. The integration over the reciprocal space was done by a $12 \times 12 \times 1$ Monkhorst–Pack sampling [27] of the Brillouin zone. We used a cutoff energy of $E_c = 544$ eV; the charge density cutoff was selected fourteen times as high. A first-order Methfessel-Paxton smearing function with a width of 0.14 eV was employed for the Cu/Ni alloy. In all DFT calculations, the relaxation converged within 10^{-4} Ry/au for each atom.

As DFT simulations of particles consisting of several hundred atoms would result in tremendous computational effort, a different strategy was adopted to study the equilibrium surface segregation behavior in the present system. Slabs consisting of ten atomic layers were constructed, with periodic boundary conditions along x and y, and two open surfaces in z direction. For (M)EAM simulations, cells with up to 4000 atoms were used. In DFT computations, supercells were constructed by stacking single Cu fcc unit cells in the z direction and adding three lattice spacings of vacuum. In all cases, the three different surfaces with lowest Miller indices have been put under scrutiny. Irrespective of the simulation approach, cell dimensions in x and y were always chosen such as to yield Cu bulk lattice constants. Periodic boundary conditions were additionally used where necessary to cross-check the potentials. Pure Cu and Ni slabs were employed to calculate surface energies. Finally, layer mixing enthalpies for bulk and subsurface placement of an atomic layer of Ni atoms were computed by replacing the sixth (bulklike) and the ninth layer (subsurface) of Cu in a slab by Ni atoms and comparing the resulting energy differences per unit area.

4. Atomic level pressures

Atomic level pressures constitute a valuable tool for the analysis of the inner stress state of nanoscaled materials. In the present work, we calculated the p_i following a well established procedure:

$$p_i = -\tfrac{1}{3}\mathrm{Tr}(\sigma_i). \tag{3}$$

The atomic level stresses $\sigma_i^{\alpha\beta}$ were derived via

$$\sigma_i^{\alpha\beta} = -\frac{1}{\Omega_i}\left(m_i v_i^{\alpha} v_i^{\beta} + \sum_j F_{ij}^{\alpha} r_{ij}^{\beta}\right). \tag{4}$$

Here, Ω_i denotes the averaged volume per atom, m_i the mass of atom i, v_i^{α} the cartesian component α of the velocity of atom i. F_{ij}^{α} describes the force between atom i and j along direction α while r_{ij}^{β} denotes the separation between atoms i and j along β.

B. Experimental details

We synthesized Ni@Cu core-shell nanoparticles via plasma gas condensation using a home-built setup described recently [9]. Details concerning the synthesis process as well as all relevant optimized parameters used in the present work can be found therein and will not be listed again. In contrast to other recent bimetallic particle studies, where CS-NPs have been produced by using supported NPs [5,28], we emphasize that our setup enables synthesis of particles in the gas phase, in absence of any substrate or additional interface. Deposition of the particles was performed after successful coating of the Ni core with a shell of Cu in presence of Ar as an inert gas at mbar pressure, directly onto lacey carbon membrane TEM grids. We performed subsequent annealing of the samples with a MILA 5000 infrared heater at pressures $p < 10^{-6}$ mbar after transport through air.

High-resolution transmission electron microscopy (HR-TEM) investigation was done using a probe-Cs corrected FEI Titan^3 G2 60-300 microscope operating at 300 kV acceleration voltage after transport of the samples under ambient conditions. We performed energy dispersive x-ray (EDX) analysis by using a FEI SuperX detector with high visibility low-background holder and collected and evaluated the data with the Bruker ESPRIT software. For EDX measurements, the microscope was set to scanning transmission electron microscopy (STEM) mode, with a beam screen current of 200 pA and a probe size FWHM down to 70 pm.

We recorded electron diffraction patterns in selected area diffraction (SAD) mode as well as in nanobeam electron diffraction (NBD) geometry [29]. Here, using a very small C2 aperture, the beam forming system in scanning mode is adjusted to create a small (down to 5-nm beam diameter), near parallel (0.18-mrad convergence semiangle) electron beam probe in order to record diffraction patterns from specific positions on the sample. This allows for seamless sequential recording of low-resolution STEM images and correlated local diffraction information.

III. RESULTS AND DISCUSSION

A. Simulating NP equilibrium structures

In this work, we focus on segregation patterns obtained far below the order/disorder transition temperature T_c, which for bulk Cu/Ni has its maximum at 630 K. Figure 1 shows the main results of our hybrid simulation runs, i.e., representative particles obtained for three different concentrations and structures at $T = 100$ K.

Several trends can clearly be identified. On the one hand, strong surface segregation of Cu atoms occurs and a monolayer of Cu covers all particles, which can be traced back to the significant difference in surface energies of the two components. While our findings suggest that surface segregation does not pronouncedly depend on concentration

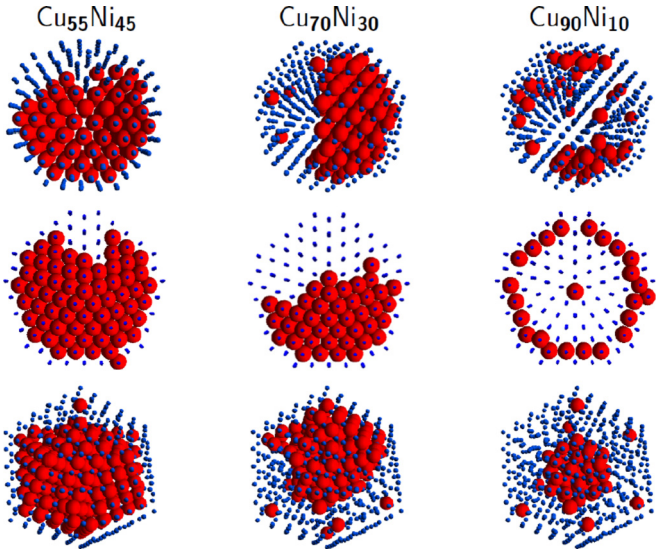

FIG. 1. (Color online) Representative segregation patterns in bimetallic Cu/Ni NPs obtained at 100 K, thus below the order/disorder transition temperature for varying concentrations (left to right) and structures (top to bottom): (a) spherical fcc crystallite with N = 532, (b) decahedron with N = 484, and (c) icosahedron with N = 561. Cu atoms are depicted in blue, Ni atoms in red.

and structure, it appears on the contrary that the specific core phase separation is strongly affected by these parameters. Single crystal and decahedral particles exhibit a low temperature JA phase, with a transition to ON structures when progressively decreasing the Ni concentration. In icosahedral particles on the other hand, a different behavior is observed: at low Ni concentrations, Ni atoms are preferentially placed in the core of the cluster. Upon increasing the concentration, a morphological instability develops, which leads to an asymmetric distribution of Ni atoms inside the NP. It is also noteworthy that–irrespective of concentration–Ni atoms are placed in the subsurface layer, right below the icosahedron vertices.

Of course, the structures presented in Fig. 1 do not necessarily represent a global energetic minimum of the system, the determination of which would require more elaborated techniques [1]. Still, being chosen from a canonical ensemble, we can consider these results being representative for typical equilibrium segregated particles. With respect to the observed structures, our findings on Cu/Ni are thus in agreement with recent predictions on other weakly miscible material systems [2,4] and further support the idea of generic demixing motifs emerging in NPs made of weakly miscible components, enabling a taxonomy of bimetallic particles along the lines of adopted segregation patterns.

With regard to the employed simulation algorithm, the agreement between our findings and previous results is not a priori obvious. Our approach, developed to ensure maximum local strain relaxation as well as fast convergence through deterministic intermediate evolution of the system, differs from classical MMC simulations. These rely on additional translational position moves to sample phase space. The difference becomes clear by approximating the expectation value of an observable $\langle A\rangle$ in the canonical ensemble (with N atoms)

$$\langle A\rangle = \frac{\sum_{\{\sigma_i\}} \int d\vec{\tilde{x}}^N \; A(\{\sigma_i\},\{\vec{\tilde{x}}\}) \; \exp(-\beta\tilde{\mathcal{H}})}{\sum_{\{\sigma_i\}} \int d\vec{\tilde{x}}^N \; \exp(-\beta\tilde{\mathcal{H}})} \tag{5}$$

as the weighted sum over all configurations σ_i (defined by a given assignement of atom types to lattice points), supplemented by displacements $\vec{\tilde{x}}$ around a given atomic configuration (for example, using a Voronoi tesselation and requiring $\vec{\tilde{x}}$ for any atom to be enclosed within the given Voronoi cell). Here, $\tilde{\mathcal{H}}$ represents the Hamiltonian of the system after integration over the momenta and $\beta = 1/k_{\mathrm{B}}T$. If the observable of interest does not depend on $\vec{\tilde{x}}$ as would be the case for an order parameter of Warren-Cowley type, for example (typically used to identify specific segregation patterns), we can write

$$\langle A\rangle = \frac{\sum_{\{\sigma_i\}} A(\{\sigma_i\}) \; \exp(-\beta\tilde{\mathcal{F}})}{\sum_{\{\sigma_i\}} \; \exp(-\beta\tilde{\mathcal{F}})}. \tag{6}$$

Thus "correct" sampling would require knowledge of the free energy, i.e., thermodynamic integration, for any given distribution σ_i of atoms in the lattice. In contrast, in our simulation scheme, the averaged internal energy over the MD run is used instead of the free energy. Thereby, entropic contributions from atomic vibrations are selectively excluded. The agreement between our results and previous findings by other groups thus indicates that vibrational entropy can be neglected in the present system when heading for equilibrium configurations. This will be examined explicitly in the next section.

B. Vibrational entropy in bimetallic NPs

Phonon densities of states and vibrational entropy have been extensively studied in elemental metallic nanocrystals [30,31]. Two essential findings were reported in computer simulations: (i) an enhancement of the low-frequency vibrational density of states and (ii) a shift of the high frequency band when compared to bulk crystals. Observation (i) was traced back to the large amount of surface atoms. Due to their low coordination number, the latter experience a change in force field, which manifests in an effective softening of the force constants. On the other hand, (ii) was attributed to the pressure increase in small nanoparticles. There, a capillary pressure inversely proportional to the NP radius gave rise to a decrease of lattice constants and an effective bond stiffening [31,32]. Recently, these studies have been extended to icosahedral particles, enabling successful structural determination [33,34]. To date, less data are available on bimetallic nanoparticles [35], especially when it comes to quantitative predictions on relevant thermodynamic properties connected to the vibrational entropy S_{vib}.

Results from the calculation of vibrational properties of bulk and elemental spherical nanocrystals for two different EAM potentials [16,19] are listed in Table I. In general, reasonable agreement is obtained between our simulation results and experimental data [36,37], although the deviation is more pronounced for Ni (<4%) than for Cu (<2%). Calculated values of excess entropies, i.e., differences between bulk and NP values, are slightly higher for Ni ($\langle\Delta S_{\mathrm{vib}}\rangle$

TABLE I. Calculated elemental bulk and NP vibrational entropies in units of k_B/at for both EAM potentials used in this study (EAM (a) [16] and EAM (b) [19]) and comparison with literature data.

	EAM (a)	EAM (b)	Expt.
Cu (bulk)	4.09	4.03	4.00
Cu (NP)	4.31	4.28	–
Ni (bulk)	3.28	3.25	3.40
Ni (NP)	3.52	3.58	–

$= 0.29 \pm 0.06\ k_B$/at) than for Cu ($\langle\Delta S_{vib}\rangle = 0.24 \pm 0.02\ k_B$/at). Although these values are somewhat larger than those reported in earlier simulations restricted to Ag nanocrystals [30], calculation of the excess heat capacity and comparison with literature data obtained with the empirical tight-binding second moment potentials of Cleri and Rosato [31] shows very good agreement, as depicted in Fig. 2. This makes us confident that the EAM parametrization by Johnson yields satisfactory results when dealing with vibrational properties of nanocrystals and we therefore chose this potential for all bimetallic NP entropy calculations.

The main results concerning the vibrational properties of bimetallic NPs are summarized in Fig. 3(b), where all results have been obtained using the concentration averaged mean entropy value of elemental particles as a reference: $\Delta S = S_{vib} - [c_{Cu}\, S^{Cu}_{vib} + (1 - c_{Cu})\, S^{Ni}_{vib}]$. Two trends can be identified. On one hand, the vibrational entropy of solid solution alloy clusters is always significantly larger than the corresponding value for segregated clusters, an effect which is most pronounced for highest Ni concentrations and decreases with increasing number of Cu atoms. On the other hand, irrespective of concentration (and restricted by the accuracy of our computational approach), we find only very small differences between the vibrational entropies of the segregated structures. A closer look at the corresponding PDOS helps in clarifying the physical origin of these effects. Careful analysis of the densities of states reveals that, although every segregated structure has a characteristic fingerprint, specific differences between CS, ON, and JA structures are restricted to the high frequency part of the spectrum. Thus, while the specific type of segregation pattern impacts the high energy peak shift as well as its magnitude, the low frequency part of the spectrum is left unaffected by the atomic arrangement inside the NP. This can be traced back to the complete coverage of all segregated structures with a single monolayer of Cu atoms.

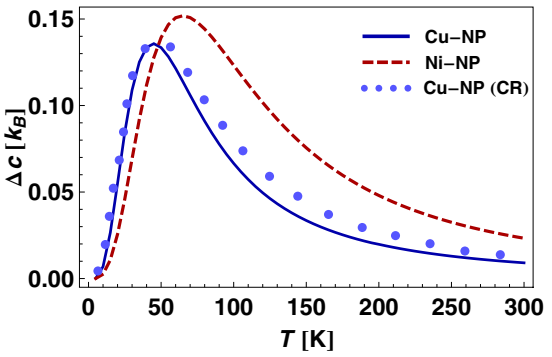

FIG. 2. (Color online) Excess specific heat calculated for Cu and Ni using the EAM (a) [16] potential. Blue dots denote available literature data [31].

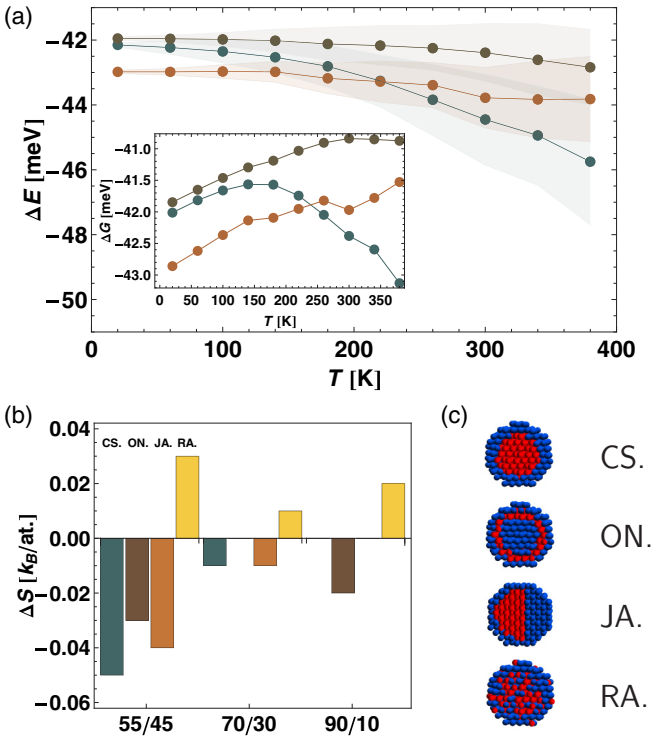

FIG. 3. (Color online) Internal energies and entropies calculated within the present study: (a) relative energy per atom of a cluster with Cu/Ni composition 55/45 and thermal fluctuations as well as free energy (inset). (b) Relative entropy change using concentration weighted elemental cluster entropy values as a reference, and (c) exemplary bimetallic clusters employed in this study (CS: core-shell, ON: onionlike, JA; januslike, RA: random distribution).

As the weighting factor of $\rho(\hbar\omega)$ in Eq.(1) is a monotonously decreasing function of the frequency, it appears that the most important contributions to the vibrational entropy must stem from low frequency modes. Thus we conclude that it is the presence of Ni atoms in the surface layer which leads to an enhanced low frequency contribution in RA particles and yields the aforementioned difference in entropy. This is consistent with its increase with the Ni concentration.

These findings can be grasped in a quantitative way by comparing internal energy contributions U, i.e., kinetic plus potential energy of the cluster, with $T\Delta S_{vib}$, the entropic contribution arising through atomic vibrations. Figure 3(a) shows the difference $\Delta E = U - U_{RA}$ for the three segregated structures analyzed herein and an averaged random configuration for an exemplary concentration $Cu_{55}Ni_{45}$. This figure reveals that the difference in internal energy, which amounts to roughly 40 meV, dominates over the vibrational entropy weighted with temperature. The same applies to differences in free energy obtained when taking configurational entropy into consideration. On the other hand, energetic differences between segregated structures are smaller by more than an order of magnitude. The inset of Fig. 3(a) shows the sum ΔG

$= \Delta E - T\Delta S_{\mathrm{vib}}$, which highlights that vibrational entropy does not result in stabilization of selected segregation patterns found below the order/disorder transition temperature. Although a transformation between CS and JA structure is predicted on purely energetic grounds, as can be seen in the same figure, the latter will not occur. This can be traced back to the impact of configurational entropy. At the JA $\rightarrow$ CS crossover temperature, this entropy already leads to mixing of the constituents due to strong depletion of Cu atoms in the particle core, as was recently demonstrated in greater detail [15].

C. The significance of onion-type segregation profiles: EAM versus MEAM and DFT calculations

As already mentioned in the introduction, ON-like equilibrium structures have been reported in a variety of simulation studies on immiscible bimetallic fcc nanocrystals relying on EAM potentials [3,4]. Here, we also identify such a segregation behavior in the Cu/Ni system when analyzing low Ni concentrations.

Interestingly, this finding can be related to an earlier controversy on the equilibrium surface composition in Cu/Ni alloys. While some studies reported an oscillatory behavior of the concentration profile in the vicinity of a flat surface, with an enrichment of Cu in the top layer and depletion in the subsurface layer [19,38], this has been seriously questioned by other authors [39]. Obviously, if subsurface Ni enrichment would take place in the presence of flat surfaces, there is reason to believe that it would result in the aforementioned ON-like profiles when considering NPs. In the present case, especially with regard to the variety of EAM studies predicting ON-like segregation, it can thus be asked to what extent semiempirical EAM potentials will yield trustworthy results when dealing with the alloying and demixing behavior of metallic systems in the vicinity of surfaces. This is a valid question as the EAM is known to suffer from difficulties in producing quantitative descriptions for surface properties of metals [13]. Furthermore, EAM predictions on nanoclusters mostly lack experimental verification so far. To our knowledge, there is no evidence supporting the presence of ON-type structures in the aforementioned material systems. In the present work, we therefore employed MEAM and *ab initio* calculations to check the significance of subsurface Ni atom placement in demixed Cu/Ni particles, as resulting from our EAM based algorithm.

While cohesive energies and lattice constants are used as input parameters in (M)EAM approaches, these quantities are calculated from first principles in DFT. In the present case, our computations yielded lattice constants of $a(\mathrm{Ni}) = 3.526$ Å and $a(\mathrm{Cu}) = 3.633$ Å, thus overestimating experimental and (M)EAM values by less than 0.5%. On the other hand, cohesive energies $E(\mathrm{Ni}) = -4.66$ eV and $E(\mathrm{Cu}) = -3.55$ eV were found slightly higher than experimental reference data. These values differ from experiments by as much as 5%—a well known problem of DFT approaches residing on the GGA-PBE exchange-correlation functional [40]. Still, the agreement is superior to recent DFT studies where larger discrepancies have been reported [40]. Despite this shortcoming, surface energies calculated with DFT were very close to experimental values for Cu ($E^{(110)} = 1.59$ J m^{-2}, $E^{(100)} = 1.524$ J m^{-2}, $E^{(111)} = 1.378$ J m^{-2}, and $E^{\mathrm{expt}} = 1.77$ J m^{-2}) as well as for Ni ($E^{(110)} = 2.240$ J m^{-2}, $E^{(100)} = 2.173$ J m^{-2}, $E^{(111)} = 1.909$ J m^{-2}, and $E^{\mathrm{expt}} = 2.24$ J m^{-2}), while the EAM potentials used herein can yield underestimations of up to 35% [41,42], when averaging over the facets with lowest Miller indices. The employed MEAM performs slightly better, but is still less close to experimental values than *ab initio* calculations [21].

Besides looking at energetic aspects, z relaxation of the atoms in the slab was studied in detail. Indeed, the miscibility gap in Cu/Ni systems is believed to result from the small lattice mismatch of roughly 3% between the two atomic species. Taking into consideration surface relaxation effects, it stands to reason that symmetry breaking in the presence of a surface might influence the miscibility behavior and deserves closer attention.

To achieve a quantitative description, the parameter $\Delta d_i = \Delta d_{i,i+1} = \frac{z_{i,i+1} - z_{\mathrm{Bulk}}}{z_{\mathrm{Bulk}}}$ was used throughout this study, representing the percentage deviation between Cu bulk lattice plane spacing values and the distance between layers i and $i+1$. In all cases scrutinized in our study, inward (negative) relaxation of surface atoms of pure Cu slabs occurred, most pronounced for (110) surfaces with smallest packing density, and decreasing for (100) and (111) facets. Although this is not the major focus of the study, we still highlight that this result stands in conflict with experimental statements, where a slight outward relaxation of the (111) surface was reported [43]. Nevertheless, more recent first-principle calculations [44] describe an inward relaxation of $d_{12} = -1.2\%$, which agrees perfectly with our findings. When comparing the results observed for the different simulation approaches, clear regularities are difficult to identify. The two EAM potentials, for example, exhibit very distinct relaxation. In contrast, for the (100) surface, for example, there is pronounced agreement between EAM(a) and the MEAM potential. Comparison of our findings with literature data reveals reasonable agreement [45]. Typically, EAM is found to overestimate the relaxation, with exception of EAM(b), which yields values astonishingly close to experiments. Nevertheless, experimental values exhibit pronounced scattering, owing to the difficulties encountered in LEED experiments on the Cu/Ni system, and some of the experimental results remain even contradictory with respect to the relaxation direction of the surface [43,46].

Having checked the relevant properties for elemental Cu (and Ni) slabs, simulations of bulk and subsurface Ni monolayers were finally performed and our results are summarized in Fig. 4. Placement of Ni into the slab is accompanied with a reduction in lattice spacing, naturally traced back to the smaller lattice constant of Ni. When placed below the surface, this effect is most dramatic, yielding an enhanced relaxation of the surface Cu layer. Here, our data complement existing studies, restricted to (100) surfaces [47]. Where available, literature results are in very good agreement with our values (compare, for example, Ref. [47] $d_{12} = -7.2\%$ and $d_{23} = -3.9\%$ with our findings $d_{12} = -7.2\%$ and $d_{23} = -4.3\%$).

As relaxation data alone do not enable any clear classification of the simulation methods with respect to their predictive power, the layer mixing enthalpies ΔE_{m} were finally calculated. These are defined as the energy differences between the two aforementioned geometries: a positive sign describes

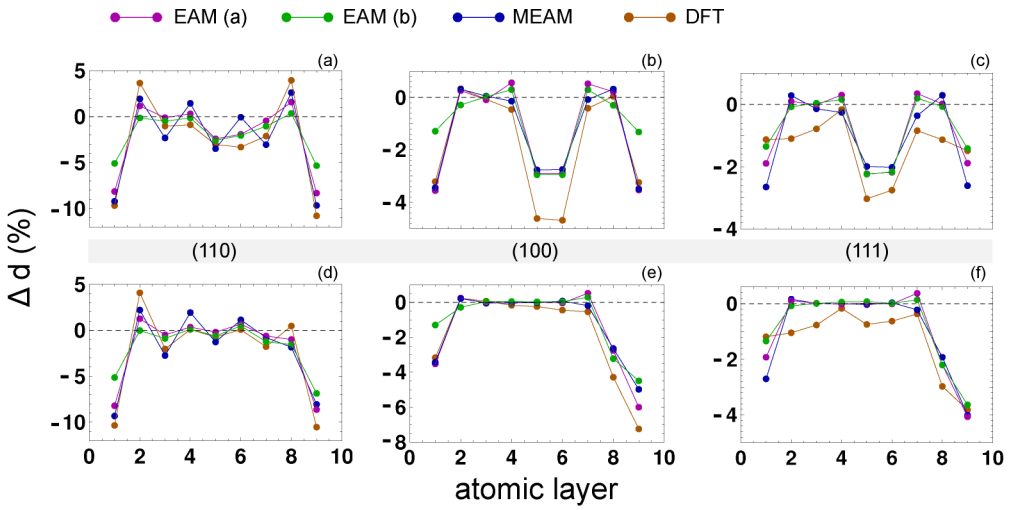

FIG. 4. (Color online) Normalized relative relaxation Δd perpendicular to the surface of the slab as a function of the atomic layer for all simulation approaches employed in the present study: (110), (100), and (111) surfaces from left to right and for bulk (a), (b), (c) vs subsurface (d), (e), (f) placement of a single layer of Ni atoms into the Cu slab.

preferential placement of Ni atoms in the subsurface layer, while a negative one would favor bulk segregation. All relevant data are listed in Table II, which summarizes the main results of this section. In contrast to relaxation data, a clear tendency emerges. While both EAM parametrizations studied herein predict subsurface Ni enrichment for all surfaces investigated, the opposite holds for MEAM and DFT calculations. This is surprising, as the relaxation behavior coincides very well for the EAM(a) potential and its MEAM counterpart, while both parametrizations yield similar bulk enthalpies of mixing equal to approximately 20 meV per atom for $Cu_{50}Ni_{50}$ composition [16,21]. This finally supports the idea that atomic relaxation alone is not sufficient to understand near surface segregation. On the contrary, electronic densities seem to play a crucial role and the redistribution of electronic charges, especially in the presence of another atomic species, must be taken into account. Although a detailed analysis of the latter is beyond the scope of the present work and will be left to future studies, our findings cast strong doubt on the relevance of EAM predictions for ON-like segregation in NPs, as the method involves an oversimplification of binding in vicinity of surfaces, relying on simple rotationally symmetric charge distribution arguments. Taking into account directional bonding seems, in the present case, to reconcile the *ab initio* approach with a semiempirical EAM philosophy. Very generally, our results lead to the conclusion that special care has to be employed when using simple EAM approaches to describe binary immiscible systems with a large number of surface atoms. Here, it would be highly desirable to cross-check previous work along the lines of this study to gain deeper insight into the significance of ON-like equilibrium structures.

TABLE II. Layer mixing enthalpy $\Delta E_m = E_{bulk} - E_{subssurf}$: comparison between EAM(a) [16], EAM(b) [19], MEAM [20], and DFT results.

		EAM (a)	EAM (b)	MEAM	DFT
$\Delta E_m^{(110)}$	(meV Å^{-2})	≈0	≈0	−4.1	−9.2
$\Delta E_m^{(100)}$	(meV Å^{-2})	5.2	4.3	−1.0	−1.2
$\Delta E_m^{(111)}$	(meV Å^{-2})	3.3	2.6	−1.6	−4.9

D. Ni@Cu CS-NP annealing studies

1. Temperature dependence of particle structure and segregation patterns

Figure 5 shows a survey of the main experimental results of the present study. STEM as well as EDX maps of representative particles are depicted for increasing annealing times and temperatures. The as-deposited particles consist of a bimodal population of elemental Ni and roughly 50% Ni@Cu CS structured particles, with a core diameter of 21 ± 3 nm and a shell with thickness 11 ± 2 nm, corresponding to typical concentrations of roughly 84 at% Cu and 16 at% Ni. All particles are surrounded by a thin oxidized layer of several nm, as becomes apparent in STEM pictures and HR-TEM image analysis. Structural properties of as-deposited NPs obtained with our setup have been extensively studied [9]. In the present work, we put the focus on the evolution of Cu and Ni atom distribution and particle microstructure with time and temperature.

Figure 5(a) shows a representative particle configuration for a sample heating time of 1.08×10^4 s (3 h) at 573 K (300 °C). Although slight Ni diffusion into the Cu shell has occurred, the CS structure is clearly preserved and can unambiguously be identified. In order to verify whether this low degree of intermixing can be considered an equilibrium effect or must be traced back to kinetic inhibition and therefore an incomplete diffusion process, the annealing time was raised by orders of magnitude to 1.04×10^6 s (12 days). The results of this experiment are depicted in Fig. 5(b). Here, in obvious contrast to Fig. 5(a), clear interdiffusion of both atomic species can be observed, although the presence of a thin Cu rim must still be considered a reminiscence of the original core-shell structure.

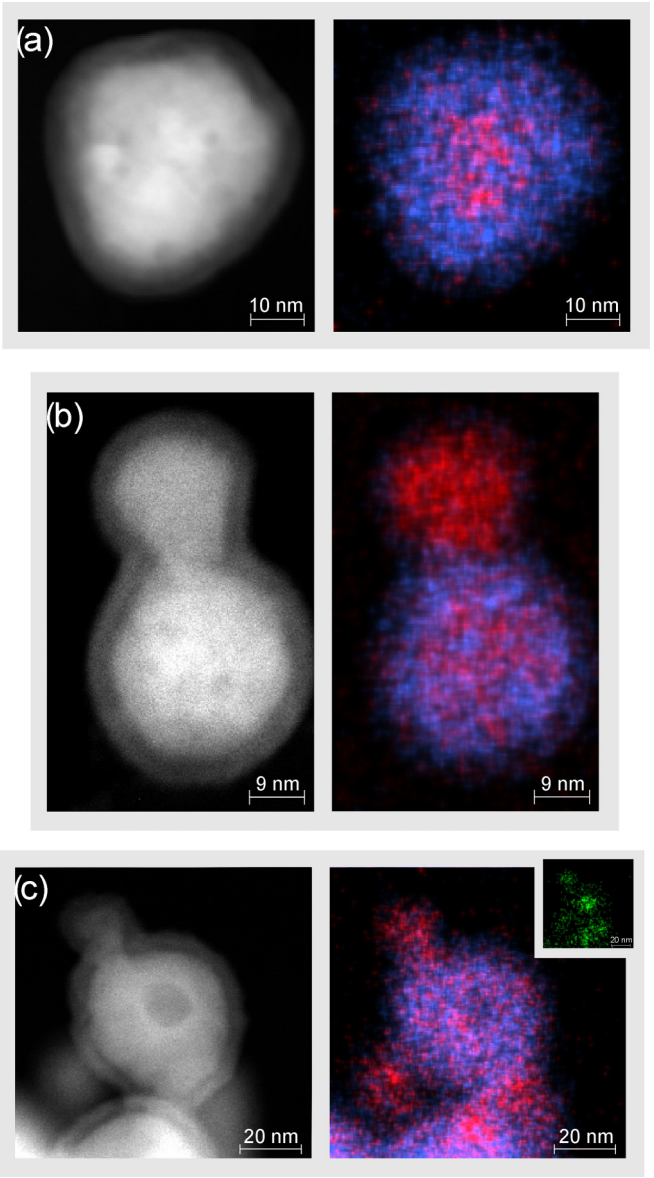

FIG. 5. (Color online) STEM micrographs (left) and EDX maps (right) of annealed CS-NPs, with increasing time and temperature from top to bottom: (a) 3 h at 300 °C, (b) 12 days at 300 °C, and (c) 3 h at 400 °C. The same color coding as in the simulation section has been used: Cu in blue, Ni in red, Fe impurities are shown in green (inset).

When increasing the temperature to 673 K (400 °C), annealing times of 1.08×10^4 s (3 h) are found sufficient to achieve complete random mixing of the particle. Surprisingly, some of these intermixed particles analyzed with STEM, exhibit a CS structure with a core possessing a much lower mass density than the surrounding shell, which is barely discernible in the EDX map [Fig. 5(c)].

To complement our STEM investigation, the atomic structure of the particles was finally assessed using HR-TEM. Uncoated Ni particles, as depicted in Fig. 6, exhibit a pronounced polycrystalline structure, as highlighted by fast Fourier transformation (FFT) of the micrographs, with characteristic grain diameters of several nm. This nanocrystalline

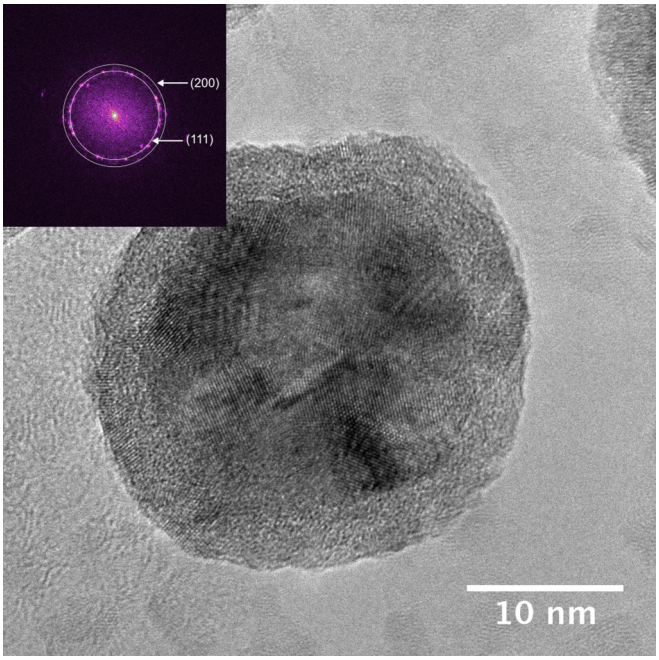

FIG. 6. (Color online) High resolution TEM picture of a Ni nanoparticle prior to coating. The pronounced polycrystallinity of the NP structure becomes apparent. Diffraction rings correspond to the (111) and (200) reflexes of a polycrystalline fcc Ni sample.

structure is also found in as-deposited CS-particles [9] and, as can be seen in Fig. 7, it is preserved after annealing to 300 °C and 400 °C. While nanodiffraction has been undertaken to assess the relative orientation of Cu shell grains to Ni core grains, results were inconclusive. While we found some evidence for textured growth of Cu on top of Ni [48], the analysis was generally severely impeded by the small difference in lattice constants between the two elements and the small grain sizes involved. A single diffraction image from a 5-nm beam diameter samples the entire cross-section of a 40-nm particle, leading to overlapping information from multiple nanocrystallites of Ni and Cu as well as the oxidized surface, making reliable quantitative predictions very difficult.

2. *Diffusion in Ni@Cu nanoparticles*

Besides unraveling equilibrium particle structures, our experiments also allow for a derivation of approximate values of temperature dependent diffusion coefficients. From almost complete interdiffusion of the species at 573 K (300 °C) after 12 days of annealing, we derive an upper bound for the diffusion coefficient by using $\langle r^2 \rangle = 6Dt$ obtaining $D < 8 \times 10^{-19}$ cm^2/s. This is in reasonable agreement with experimental results relying on Ni tracer atom diffusion in Cu $D^{\mathrm{Ni}\rightarrow\mathrm{Cu}}_{300\,^\circ\mathrm{C}} \approx 3 \times 10^{-19}$ cm^2/s estimated from data gained by Bonzel *et al.* [49]. Still, one must bear in mind that experimental data in this temperature regime is scarce, and extrapolation of high-temperature results can yield values reduced by over an order of magnitude [50]. Unfortunately, no direct volume interdiffusion data were available for this temperature regime. With respect to the rather low Ni concentration of the NPs, and considering that Cu diffusion into Ni is slower than Ni diffusion into Cu [50], it nevertheless seems reasonable to

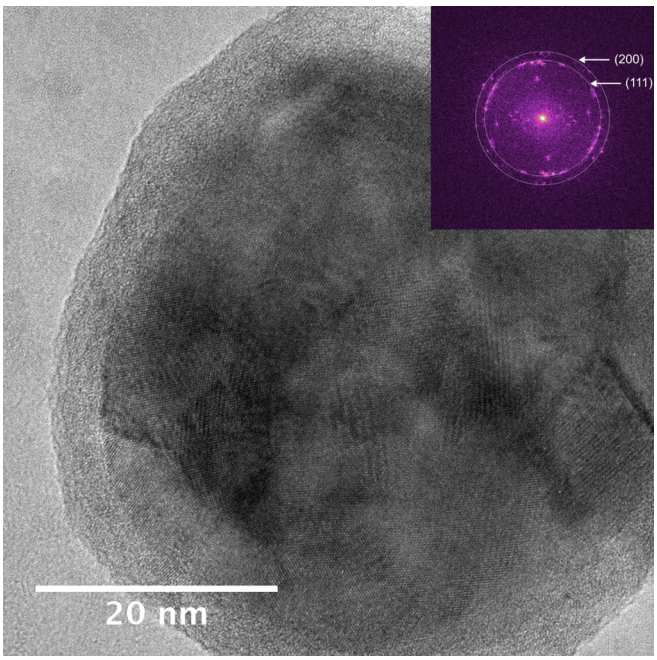

FIG. 7. (Color online) High-resolution TEM micrograph of a Ni@Cu NP after annealing for 12 days at 300 °C. The particle still exhibits a nanocrystalline structure. The theoretical (111) and (200) maxima for a polycrystalline fcc structure of lattice constant $a = 3.57$ Å have been indicated by rings in the FFT. Since the expected fcc lattice constants of Cu ($a = 3.62$ Å) and Ni ($a = 3.52$ Å) are very close, there is pronounced overlap in the experimental core-shell image. Additional contributions to the FFT stem from the amorphous and semicrystalline oxide surface.

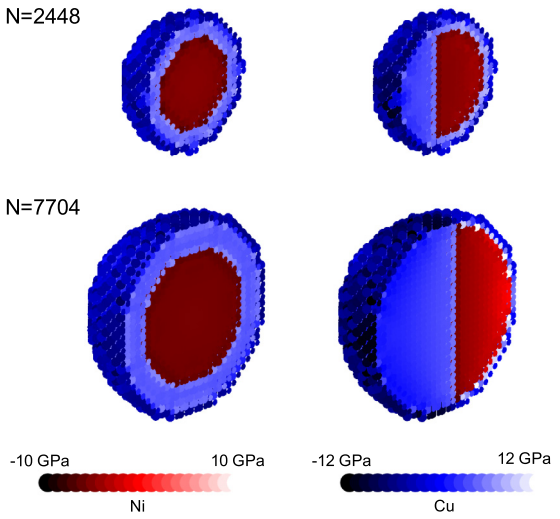

FIG. 8. (Color online) Atomic level pressures with increasing particle size highlighting increased stress release in JA-like particles in comparison to CS structures with growing NP radius.

use $D^{\mathrm{Ni}\to\mathrm{Cu}}$ for comparison. This is further supported by diffusion data of tracer Ni in Cu/Ni alloys (78.5 at% Cu), where high-temperature experiments above 800 °C show very little difference to diffusion in pure Cu [50]. With this, using the aforementioned bulk volume diffusion coefficients of dilute Ni in Cu, the typical time for complete intermixing of a CS-NP at 673 K (400 °C) can be estimated and is found to be 8×10^3 s, which is compatible with the diffusion time observed in our annealing experiments.

It is noteworthy to realize that these values lie several orders of magnitude below results from measurements of grain boundary (GB) diffusion in Cu/Ni [51]. In Cu/Ni thin film couples interdiffusion in the temperature range 573 K $< T <$ 777 K was found characterized principally by type B kinetics, i.e., a fast GB diffusion followed by diffusion into the grain interiors, with typical values exceeding by far previously reported bulk data [52]. Surprisingly, in our experiments, although we cannot exclude GB contributions as well as surface diffusion, we do not observe such an enhancement and our estimated diffusion coefficients are in agreement with the aforementioned bulk data.

E. Comparing simulations and experiments

1. *Equilibrium segregation and nanocrystallinity*

A detailed comparison between theoretical predictions and experiments remains challenging in the field of multicomponent NPs. In the present case, the first difficulty arises from the fact that simulated and synthesized particles differ in size by roughly an order of magnitude. While this seems a knockout criterion at first sight, we believe that results gained on nanoclusters can cautiously be extrapolated to larger nanocrystals. First, from a theoretical point of view, it must be highlighted that icosahedral structures can be ruled out when considering the particle sizes described in the present study. Icosahedral structuring results in pronounced lattice strains, energetically penalizing these NPs and making decahedral and single-crystalline motifs more likely with increasing size. In elemental Ni NPs, for example, the typical crossover size from an icosahedron to a decahedron and later on to a single crystal obtained via Wulff-construction was calculated as 2300 and 17 000 atoms, respectively [53].

To extrapolate results on single crystalline clusters to larger sizes, we analyzed the distribution of atomic level pressures p, as shown in Fig. 8 for spherical JA and CS nanocrystals with same concentration and varying size. While in previous sections, we could show that the Cu/Ni system will favor a JA-like arrangement for small fcc-nanocrystal sizes (as accessible to our MMC simulations), a detailed analysis of the p_i shows that this must still hold with increasing number of atoms. Indeed, JA configurations give rise to lower interfacial stresses and with increasing particle radius, a clear pressure reduction can be achieved. In contrast, for CS-NPs, the lattice mismatch in the Cu/Ni system yields a pronounced pulling on the Ni core as well as a compression of the shell, which increases with particle size and makes this arrangement clearly energetically unfavorable.

Nevertheless, this argumentation only holds for single-crystalline clusters. As highlighted in the previous section, the nanoparticles grown in our study exhibit pronounced nanocrystalline characteristics. To study the impact of grain boundaries onto the segregation behavior in the clusters, we thus performed hybrid MD/MMC runs on particles with a twist grain boundary.

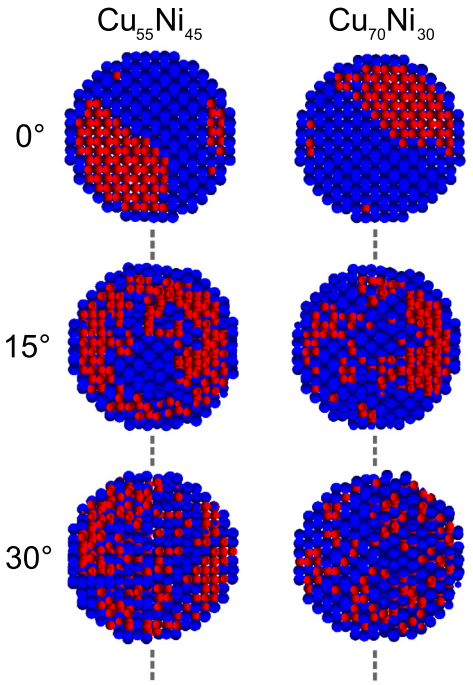

FIG. 9. (Color online) NP equilibrium configurations after approximately 1.5×10^5 MMC/MD steps as a function of the twist boundary angle and concentration at 100 K. Twist boundary planes divide the particles in two halves with equal number of atoms—the cutting plane in the above pictures is perpendicular to the twist boundary plane, which is marked with a dashed line.

Exemplary results of these simulations for varying twist boundary angles and concentrations are shown in Fig. 9. While single crystalline particles exhibit the expected JA behavior, presence of high angle grain boundaries clearly affect the segregation. For a twisting angle of 30°, we find the demixing tendency of the two species to be almost completely suppressed. This yields strong evidence for the possibility of low-temperature segregation hindrance in nanocrystalline Cu/Ni particles.

With respect to the concentrations analyzed in our experiments, the expected bulk order-disorder transition temperature T_c has been predicted to lie approximately in the range 480–630 K, depending on the reference study [54,55]. Excluding a size induced reduction of T_c, which should play a minor role in particles of more than 20 nm radius [56,57], we eventually ascribe the absence of CS → JA transition to the small miscibility gap in Cu/Ni combined with a pronounced nanocrystallinity of the NPs.

2. *Oxidation in ternary Cu/Ni/Fe NPs*

As already reported in a previous section, STEM results, as shown in Fig. 8(c), hint at a dramatic microstructural change when annealing the samples to 400 °C. While the low contrast inside the particles suggests a hollow core, as observed in many oxidized NP systems and theoretically explained by the Kirkendall effect [58], a different mechanism is at work in the present system. Indeed, careful analysis of EDX spectra unveils a very small amount of iron impurities present in the particle. During synthesis, Ni NPs partly incorporate residual Fe, which stems from accidental sputtering of the magnetron gun. While the amount of impurities lies below 3% in the mixed particles exhibiting a hollow core, its presence seems sufficient to induce the creation of a small oxidized iron core with few nm radius, as confirmed through EDX mapping. Attempts to simulate this behavior in ternary Cu/Ni/Fe nanoparticles using a recently developed EAM potential [59] in combination with our hybrid MD/MMC algorithm failed in reproducing Fe@CuNi NPs. This suggests that iron oxidation plays a key role in the development of these CS structures.

IV. CONCLUSION

In the present study, we investigated the segregation behavior of bimetallic Cu/Ni nanoparticles using a combined experimental/simulation study. Our findings highlight how this material system with a weak miscibility gap is dominated by binding energetics and configurational entropy alone. We show in detail that vibrational entropy does not impact the segregation behavior. Along these lines, we additionally demonstrate that below the order/disorder transition, JA-like structures have to be expected in nanocrystals (and decahedral NPs). In contrast, icosahedral particles exhibit a preferential CS arrangement, with a morphological instability above a critical concentration, which has already been reported for a variety of other bimetallic NPs [2]. The presence of ON-like structures is ruled out by comparison of our results with MEAM and DFT simulations, which highlights the possible shortcomings of the EAM.

With regard to experiments, we show that an annealing of CS-structured particles yields complete intermixing of the constituents and the absence of expected JA particles above 573 K (300 °C). This can be ascribed to the pronounced polycrystalline structure of the studied NPs as well as the small miscibility gap in the Cu/Ni system. Segregation patterns at lower temperatures were found inaccessible, due to large diffusion times. Analysis of the calculated diffusion coefficients in NPs with typical radii around 20 nm finally unravel a bulk-like annealing behavior. Computer modeling of this dynamical process in order to understand the dependency of diffusion upon particle structure is subject to current research.

ACKNOWLEDGMENTS

We would like to thank E. Wisotzki for proofreading the manuscript and B. Rauschenbach for general support. This project is funded by the Deutsche Forschungsgemeinschaft (DFG)-Priority Programme 1681 "Field controlled particle matrix interactions: synthesis multiscale modelling and application of magnetic hybrid materials," as well as by the Leipzig Graduate School of Natural Sciences "Building with Molecules and Nano Objects" (BuildMoNa). Financial support of the European Union and the Free State of Saxony (LenA project; Project No. 100074065) is also gratefully acknowledged.

[1] R. Ferrando, J. Jellinek, and R. L. Johnston, Chem. Rev. **108**, 845 (2008).

[2] D. Bochicchio and R. Ferrando, Phys. Rev. B **87**, 165435 (2013).

[3] A. A. Dzhurakhalov and M. Hou, Phys. Rev. B **76**, 045429 (2007).
[4] Y. Wang and M. Hou, J. Phys. Chem. C **116**, 10814 (2012).
[5] C. Langlois, Z. L. Li, J. Yuan, D. Alloyeau, J. Nelayah, D. Bochicchio, R. Ferrando, and C. Ricolleau, Nanoscale **4**, 3381 (2012).
[6] R. Ferrando, J. Phys. Condens. Matter **27**, 013003 (2015).
[7] C. S. Kumar and F. Mohammad, Adv. Drug Delivery Rev. **63**, 789 (2011).
[8] V. Velasco, D. Pohl, A. Surrey, A. Bonatto-Minella, A. Hernando, P. Crespo, and B. Rellinghaus, Nanotechnol. **25**, 215703 (2014).
[9] M. Hennes, A. Lotnyk, and S. G. Mayr, Beilstein J. Nanotechnol. **5**, 466 (2014).
[10] J. Chatterjee, M. Bettge, Y. Haik, and C. J. Chen, J. Magn. Magn. Mater. **293**, 303 (2005).
[11] J. Ahmed, K. V. Ramanujachary, S. E. Lofland, A. Furiato, G. Gupta, S. Shivaprasad, and A. K. Ganguli, Colloids Surf. A **331**, 206 (2008).
[12] Y. Wu, J. Fowlkes, and P. Rack, J. Mater. Res. **26**, 277 (2011).
[13] M. S. Daw, S. M. Foiles, and M. I. Baskes, Mater. Sci. Rep. **9**, 251 (1993).
[14] M. I. Baskes, Phys. Rev. B **46**, 2727 (1992).
[15] M. Hennes, J. Buchwald, and S. G. Mayr, CrystEngComm **14**, 7633 (2012).
[16] R. A. Johnson, Phys. Rev. B **39**, 12554 (1989).
[17] https://staff.aist.go.jp/h.ogawa/npstudio/indexe.html
[18] B. Fultz, Prog. Mater. Sci. **55**, 247 (2010).
[19] S. M. Foiles, Phys. Rev. B **32**, 7685 (1985).
[20] B.-J. Lee, J.-H. Shim, and M. I. Baskes, Phys. Rev. B **68**, 144112 (2003).
[21] B.-J. Lee and J.-H. Shim, CALPHAD **28**, 125 (2004).
[22] http://lammps.sandia.gov
[23] P. Giannozzi, S. Baroni, N. Bonini, M. Calandra, R. Car, C. Cavazzoni, D. Ceresoli, G. L. Chiarotti, M. Cococcioni, I. Dabo, A. Dal Corso, S. de Gironcoli, S. Fabris, G. Fratesi, R. Gebauer, U. Gerstmann, C. Gougoussis, A. Kokalj, M. Lazzeri, L. Martin-Samos, N. Marzari, F. Mauri, R. Mazzarello, S. Paolini, A. Pasquarello, L. Paulatto, C. Sbraccia, S. Scandolo, G. Sclauzero, A. P. Seitsonen, A. Smogunov, P. Umari, and R. M. Wentzcovitch, J. Phys. Condens. Matter **21**, 395502 (2009).
[24] Au.pbe-nd-van.UPF, Ni.pbe-nd-rrkjus.UPF, Cu.pbe-n-van_ak.UPF
[25] http://www.quantum-espresso.org
[26] J. P. Perdew, K. Burke, and M. Ernzerhof, Phys. Rev. Lett. **77**, 3865 (1996).
[27] H. J. Monkhorst and J. D. Pack, Phys. Rev. B **13**, 5188 (1976).
[28] M. Benoit, C. Langlois, N. Combe, H. Tang, and M.-J. Casanove, Phys. Rev. B **86**, 075460 (2012).
[29] J. Zuo, M. Gao, J. Tao, B. Li, R. Twesten, and I. Petrov, Microsc. Res. Tech. **64**, 347 (2004).
[30] A. Kara and T. S. Rahman, Phys. Rev. Lett. **81**, 1453 (1998).
[31] R. Meyer, L. J. Lewis, S. Prakash, and P. Entel, Phys. Rev. B **68**, 104303 (2003).
[32] R. Meyer, S. Prakash, and P. Entel, Phase Transitions **75**, 51 (2002).
[33] H. Lei, J. Li, Y. Liu, and X. Liu, Europhys. Lett. **101**, 46001 (2013).
[34] H. E. Sauceda and I. L. Garzón, Phys. Chem. Chem. Phys. (2015), doi: 10.1039/C5CP00232J.
[35] F. Calvo, J. Phys. Chem. C **115**, 17730 (2011).
[36] P. D. Bogdanoff, T. L. Swan-Wood, and B. Fultz, Phys. Rev. B **68**, 014301 (2003).
[37] M. S. Lucas, L. Mauger, J. A. Muñoz, I. Halevy, J. Horwath, S. L. Semiatin, S. O. Leontsev, M. B. Stone, D. L. Abernathy, Y. Xiao, P. Chow, and B. Fultz, J. Appl. Phys. **113**, 17A308 (2013).
[38] H. Y. Wang, R. Najafabadi, D. J. Srolovitz, and R. LeSar, Phys. Rev. B **45**, 12028 (1992).
[39] S. Ouannasser, L. T. Wille, and H. Dreyssé, Phys. Rev. B **55**, 14245 (1997).
[40] R. Nazarov, T. Hickel, and J. Neugebauer, Phys. Rev. B **85**, 144118 (2012).
[41] S. M. Foiles, M. I. Baskes, and M. S. Daw, Phys. Rev. B **33**, 7983 (1986).
[42] R. A. Johnson, Phys. Rev. B **37**, 3924 (1988).
[43] I. Bartoš, P. Jaroš, A. Barbieri, M. A. Van Hove, W. F. Chung, Q. Cai, and M. S. Altman, Surf. Rev. Lett. **02**, 477 (1995).
[44] J. L. D. Silva, C. Stampfl, and M. Scheffler, Surf. Sci. **600**, 703 (2006).
[45] J. Wan, Y. L. Fan, D. W. Gong, S. G. Shen, and X. Q. Fan, Modell. Simul. Mater. Sci. Eng. **7**, 189 (1999).
[46] S. A. Lindgren, L. Walldén, J. Rundgren, and P. Westrin, Phys. Rev. B **29**, 576 (1984).
[47] D. Spisák and J. Hafner, J. Phys. Condens. Matter **12**, L139 (2000).
[48] See Supplemental Material at http://link.aps.org/supplemental/10.1103/PhysRevB.91.245401 for results on NBD.
[49] H. P. Bonzel, Ber. Bunsen-Ges. Phys. Chem. **70**, 73 (1966).
[50] D. B. Butrymowicz, J. R. Manning, and M. E. Read, J. Phys. Chem. Ref. Data **5**, 103 (1976).
[51] H. Lefakis, J. Cain, and P. Ho, Thin Solid Films **101**, 207 (1983).
[52] B. C. Johnson, C. L. Bauer, and A. G. Jordan, J. Appl. Phys. **59**, 1147 (1986).
[53] C. L. Cleveland and U. Landman, J. Chem. Phys. **94**, 7376 (1991).
[54] S. an Mey, CALPHAD **16**, 255 (1992).
[55] S. Srikanth and K. T. Jacob, Mater. Sci. Technol. **5**, 427 (1989).
[56] A. Christensen, P. Stoltze, and J. K. Norskov, J. Phys. Condens. Matter **7**, 1047 (1995).
[57] J. Weissmüller and C. Lemier, Philos. Mag. Lett. **80**, 411 (2000).
[58] H. J. Fan, U. Gösele, and M. Zacharias, Small **3**, 1660 (2007).
[59] G. Bonny, R. Pasianot, and L. Malerba, Philos. Mag. **89**, 3451 (2009).